Granular jet impingement on a fixed target

Yrjö Jun Huang (黃駿),[1,2,*] C. K. Chan,[1] and Piroz Zamankhan[3]

[1]*Department of Applied Mathematics, The Hong Kong Polytechnic University, Hung Hom, Kowloon, Hong Kong, China*
[2]*Department of Energy and Process Engineering, Norwegian University of Science and Technology, Trondheim, Norway*
[3]*Faculty of Industrial, Mechanical Engineering and Computer Sciences, University of Iceland, Reykjavík, Iceland*

In this work discrete element modeling (DEM) was applied to the flow of granular jets against a target. The resulting sheetlike or conelike formations under different conditions are described and explained by means of kinetic analysis. A qualitative and quantitative comparison with experimental results [Cheng *et al.*, Phys. Rev. Lett. **93**, 188001 (2007)] provides interesting insights in the theoretical treatment of the head-on collision of granular jets. Results presented in this paper provide a theoretical description of this type of physical system. However, there still exist obstacles in obtaining quantitative results.

PACS number(s): 45.70.Mg, 83.80.Fg

I. INTRODUCTION

Granular flows have received considerable attention during the past few decades because granular materials are commonly used in various industries and in daily life. The major hindrance in predicting flow of grains accurately is possibly that there has not been an accepted set of fundamental equations until now [1,2]. This difficulty originates from some fundamental characteristics of granular materials, such as dissipative collisions, and a lack of scale separation between mesoscopic single particles and the macroscopic flow [3].

Grains in a granular flow experience resistance forces from the interstitial air. Recent experiments [4–7] highlighted that the interstitial air plays a role in the systems comprised of very small grains. However, the drag force caused by the viscous interaction with the air may be considered small when the particle diameter is greater than 250 μm [8]. In these cases, the flow field is mainly controlled by the transport of momentum via direct (frictional and collisional inelastic) contacts between the grains [9].

Due to the relative velocity between the particles, granular media motions is often classified into three regimes, gaseous, liquid, and solid phases, namely, rapid granular (collisional) flows, dense shear flows and jammed states, respectively [10–12]. The solid volume fraction, Φ, and the coefficients of restitution (COR), both in normal and tangential directions, are important parameters in describing the state of granular flow [2]. There is a critical volume fraction, Φ_c, which separates the rapid gaseous phase from the other two regimes. For $\Phi < \Phi_c$, the granular flow is believed to be considerably described by the Navier-Stokes model supported by the Boltzmann-Enskog kinetic theory [12]. In this case, the viscosity is a function of the granular temperature and the temperature depends on the shear rate [13]. A number of studies have been carried out using kinetic theories for modeling in fast rapid states [14–16]. The basis of kinetic theory is the assumption of binary collisions between particles.

On the other hand, for at high volume fractions, $\Phi > \Phi_c$, the granular material performs could behave like Bingham viscoelastic material. In this case, the material behaves as a viscoelastic body at low stress while flows at high stress [8]. There may be a significant change in bulk behavior due to the development of a granular chains within the bulk [17]. A number of phenomena such as dilatancy [18], jamming [19], shear localization [20], can be induced by aggregation of grains into clusters. It may be speculated that a granular flow results from the breakdown of the weakly connected aggregates. At high pressure, the granular flow is a consequence of the rupture of strongly connected aggregates and resistance to the deformation of networks. Due to the strong nonlinear characterize of the granular cluster, some mathematical description were presented but with very strict limitation for the dense granular flow and the transition process between the solid and liquid states, such as depth-averaged method for shallow free surface flows [21,22]. Most of the research on the transition process for deep granular flows, e.g., packing and jamming in granular hopper flow in a silo, were carried out by experiments [23,24] and simulations [25–28].

Note that the adequate boundary conditions and initial conditions for time-dependent flows such as granular jet impingement on a fixed target Cheng *et al.* [29] with abrupt changes are not clearly known. The granular jet is an important phenomenon in industry. A downward continuous jet against an obstacle forms a heap with avalanches on the surface. A shock forms at the front of the obstacle and it is also affected by the shape of the obstacle [30,31]. Experimental results have demonstrated that fast moving surfaces produce sheets or cones at high initial velocities [29].

Numerical simulations have become important tools in the research of dense granular flow. DEM is one of the most widely used methods in the simulation of dense granular flows. Key features of the granular jets can be captured to provide details that are helpful in the development of accurate models for granular flow. Several DEM models have been proposed to describe the changes of velocity due to collisions or contacts [32–34]. In this paper, DEM is used to simulate granular jets impacting on obstacles and the results are compared with those acquired from experiments.

The structure of this paper is as follows. Section II gives a brief introduction of the experiments [29] as well as the details of the computational model. Section III provides further details of computer simulations. In Sec. IV, a kinetic
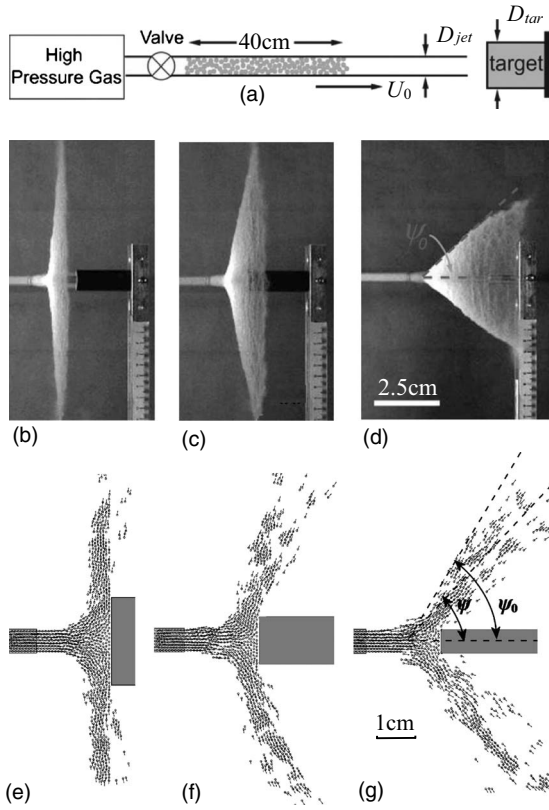
*jun.huang@ntnu.no

FIG. 1. Scattering patterns with different sizes of targets: (a) experimental setup; (b)–(d) experimental results with the same scale and (e)–(g) computed results with the same scale. Here, the experimental patterns are courtesy from Ref. [29].

analysis is used to explain the phenomenon observed in experiments and reproduced in simulation. The comparisons of theoretical analysis and experiments are presented in Sec. V. Conclusions are drawn in Sec. VI.

II. PROBLEM DESCRIPTION AND METHODOLOGY

The experimental setup of Cheng *et al.*'s [29] is shown in Fig. 1(a). Spherical glass or copper beads of sizes varying from 0.05 to 2 mm were packed in a tube with an inner diameter of 0.73 cm. Pressurized gas drove the granular plug into a jet that hit the center of the top surface of a cylindrical target with diameter D_{tar}=2.5 cm. The jet kept its cylindrical shape until very close to the obstacle and it deformed into an extraordinarily thin symmetric granular sheet if the size of the bead was small and the diameter of the obstacle, D_{tar}, was much larger than the size of the beads. With decreasing D_{tar}, the sheets change into cones. It has been shown that the opening angle of the cone Ψ_0 depends on $(D_{tar}/D_{jet})^2$ when $\Psi_0 < 90°$. The experiments shown in Figs. 1(b)–1(d) indicate that the glass or copper beads produce similar behavior. In addition, with the increase in beads size, the sheet diverged and the trajectories performed like fireworks, as shown in Figs. 2(a) and 2(b).

In this paper, parameters of the physical geometry and particles in the DEM simulation are similar to those shown in the experiments of Cheng *et al.* [29]. The surface rough-
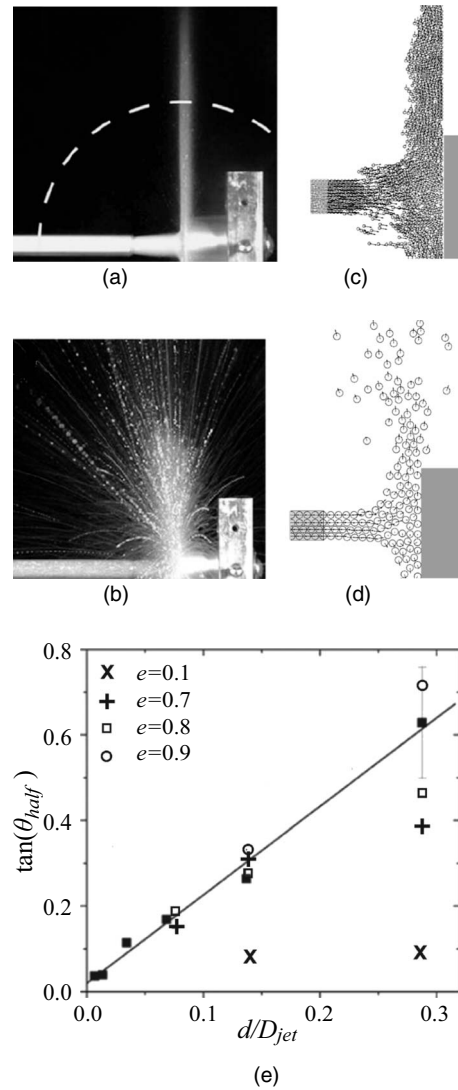

FIG. 2. Scattering patterns with different sizes of particles: (a) experiment using fine particle; (b) experiment using coarse particle; (c) simulation with fine particle; (d) simulation with coarse particle and (e) comparison of experimental and simulated results. The experimental results with $e=0.8 \pm 0.05$ are shown in ■. The experimental patterns are courtesy from Ref. [29].

ness of the particles was assumed to be $\mu=0.2$, while the coefficient of restitution in the normal direction was kept as a constant. Since the computational expense increases with the number of particle, a simplified two-dimensional (2D) model was used to reproduce the three-dimensional (3D) experiments. The motions of these spherical particles were limited in a 2D plain. In other words, only three degrees of freedom are considered, two for translations and one for rotation in the simulations.

The DEM, namely, soft-particle model, was first developed by Cundall for the analysis of rock-mechanics problems [35] and then applied to soils by Cundall and Strack [36]. The DEM algorithms allow finite displacement and rotation of discrete particles. Moreover, they should be able to detect the contacts among particles automatically. These requirements referring for DEM is also met by event-driven

method (EDM), namely, hard particle model [37,38]. In order to distringas the soft-particle model from EDM, the terms *time driven model* (TDM) and *distinct element model* are also used for the soft-particle model. A DEM algorithm given by Ramírez *et al.* [32] was chosen in our simulations so that the particle-particle collision process could be modeled as a spring-dashpot system. Hence, the normal interaction force was the sum of an elastic term and a viscous term, given by

$$F_n = F_n^e + F_n^d = K_n \delta_n^\zeta + \eta_n \delta_n^\xi \dot{\delta}_n, \qquad (1)$$

where δ is the overlap, K_n is the effective stiffness and η_n is the damping coefficient. By means of dimensionless analysis of Hertz's theory [41], it is shown that $\zeta = 3/2$. In addition, Kuwabara and Kono pointed out that $\xi = 0.5$ [33]. A value for the COR in the normal direction, $e = 0.8 \pm 0.05$, was mentioned for glass beads in the experiments [29]. In order to keep e as the aforementioned value in the simulations as well as the experiments, the stiffness coefficient is given by $K_n = \frac{4}{3} Y_{eff} \sqrt{r_{eff}}$ [39], and the damping coefficient is given as a function related to e, that $\eta_n = -2\kappa \sqrt{(5k_n m_{eff})/6}$ [42]. Here, Y_{eff} is the effective Young's modulus given by $Y_{eff} = Y/2(1-v^2)$, where Y is the Young's modulus, v is the Poisson's ratio and the subscripts 1 and 2 indicate the two colliding particles, respectively. r_{eff} and m_{eff} are effective radius and effective mass, given by $r_{eff} = (\frac{1}{r_1} + \frac{1}{r_2})^{-1}$ and $m_{eff} = (\frac{1}{m_1} + \frac{1}{m_2})^{-1}$. κ is the damping coefficient associated to the dashpot and COR in normal, e, that $\kappa = \frac{\ln(e)}{\sqrt{\ln^2 e + \pi^2}}$. k_n is given as $k_n = 2 Y_{eff} \sqrt{r_{eff}}$. For glass, density $\rho = 2500$ kg/m³, $Y = 6.5 \times 10^{10}$ Pa and $v = 0.244$ were used in the simulations [40].

The tangential force was obtained from the Coulomb's friction law that $|\mathbf{F}_{t,i}| = \mu |\mathbf{F}_{n,i}|$. The normal and tangential components of impulse were given by $\mathbf{J}_n = \mathbf{F}_n dt$ and $\mathbf{J}_t = \mathbf{F}_t dt$, where dt is the time step. Considering the balance of impulse and exchanges of velocities due to collisions with all particles in contact, the velocities after the time step dt are given by

$$\mathbf{U}'_{n,t} = \mathbf{U}_{n,t} + \frac{\Sigma \mathbf{J}_{n,t}}{m}, \qquad (2)$$

$$\mathbf{\Omega}' = \mathbf{\Omega} + \frac{\Sigma \mathbf{J}_t}{I}, \qquad (3)$$

where the prime means the status at the end of the time step, the corresponding symbols without prime are the status at the beginning of the time step and I is the momentum of inertia. Substituting the radius, r, of each spherical particle into the equation $I = 0.4 m r^2$ leads to the corresponding momentum of inertia. The contact model between the particle and the target is the same as that between particles. Due to the lack of the material parameters for the target, they were assumed to be the same as those of the particles, but the diameter and mass of the target were infinite. Hence, both the effective mass m_{eff} and the effective radius r_{eff} equal to those for binary collision. Because the interaction between the particles and tube was not considered in our simulations, the particles were assumed to propagate with a uniform axial velocity

without radical and angular velocities in the tube. In addition, in order to avoid collision in the tube, which may disturb the uniform velocity field, there is a very tiny gap between every two neighboring particles, as well as those particles to the tube.

Time step is a very important parameter in DEM simulation. A huge time step may lead to large free-flight distance and overlap. Substituting such unreasonable overlap into Eq. (1) causes a huge normal interaction force. Thus the collision does not obey the law of energy conservation more. On the contrary, a smaller time step consumes more CPU time. According to Ji and Shen [34] the time step should be less than 2% of the shortest binary contact time. For elastic binary collision, Hertz used the stiffness coefficient K_n as a function of overlap, δ_n, and pointed out that the contact time, t_c, is a function of the relative velocity given by $t_c = 2.87 (\frac{m_{eff}^2}{r_{eff} Y_{eff}^2 |\mathbf{U}|_n})^{0.2}$ [41]. If the collision is inelastic and COR in normal, e, is supposed to be a constant, then the contact time for the collision model as described by Eq. (1) may be given as [43,44],

$$t_c = \frac{\pi}{\sqrt{(2K_n/m_{eff})(1-\kappa^2)}}. \qquad (4)$$

Thus the contact time is independent of the impact velocity but dependent on the COR in the normal direction, e, in the spring-dashpot model described by Eq. (1). When e is zero, not only the contact time but also the viscous term approaches infinite. Therefore this model cannot be used for completely plastic collisions. On the other hand, to avoid some unreasonable overlap, the maximum flight distance is also an important aspect in selecting the time step, that

$$|\mathbf{u}|_{max} dt \ll \delta_{max}. \qquad (5)$$

The detail of the dimensionless overlap δ^*, the ratio between the deformation of one particle, $\frac{1}{2}\delta$, and the diameter d, is discussed in Sec. V. It was required that $|\mathbf{u}|_{max} dt < 1 \times 10^{-4} d$ in our simulations.

III. NUMERICAL SIMULATIONS

Figures 1(b)–1(d) illustrate the side views of granular jets at velocity $U_0 = 10$ m/s. The nondimensional target sizes $R_{tar}^* = D_{tar}/D_{jet}$ were set at 2.0, 1.62, and 0.88, respectively. The cone angle Ψ_0 increases linearly with R_{tar}^* until it approaches 90°. Simulation was carried out by means of DEM and the results are presented in the Figs. 1(e)–1(g) with $R_{tar}^* = 3.0$. 2.0 and 1.0, respectively. Due to the limitation of computation power, the smallest particle used in the experiments was not simulated. The diameters of the particles in the simulations were selected from $d = 0.25$ mm to 2 mm.

Using Eq. (4), the contact times for the particles with diameters 0.25, 0.5, 1, and 2 mm are 2.98×10^{-8}, 6.96×10^{-8}, 1.67×10^{-7}, and 3.97×10^{-7} s, respectively. The corresponding time steps, dt, are 5.86×10^{-10}, 1.39×10^{-9}, 3.34×10^{-9}, and 7.95×10^{-9} s respectively. All these time steps are small enough to satisfy the requirement of $|\mathbf{u}|_{max} dt < 1 \times 10^{-4} d$.

Similar to those shown in Figs. 1(a)–1(d), Figs. 2(a) and 2(b) are also courtesy from Ref. [29], which illustrated the

qualitative changes in the particle trajectories as d/D_{jet} increased. Figures 2(c) and 2(d) show the scattering patterns from our DEM simulations. Both experiments and simulations illustrated in Fig. 2(e) show $\tan(\theta_{half})$ increases with the dimensionless particle size of d/D_{jet}. In addition, the simulations indicate that the COR in the normal direction e affects the characterizing scattering angle, θ_{half}. This angle is defined as the minimal value of $\theta_2 - \theta_1$, in which half of the total particles are involved. There is somehow disagreement between the simulations and experiments. This maybe is because of the parameters selection. For example, COR in the normal direction is not a constant, but affected by the size and velocity of particle [45].

IV. KINETIC ANALYSIS

The discrete property of the granular material determines that it cannot be considered as continuous media at the particle size scale. The contact force can be presented by DEM simulation in microscale. Through statistical averaging of the contact force, the macrostresses can be determined. The macrostresses σ_{ij} is composed of two parts, the contact stress, $\sigma_{ij}^c = \frac{1}{A} \Sigma_{k=1}^N \Sigma_{l=1}^{N_k} (F_j^{kl} r_i^{kl})$, and the kinetic stress, $\sigma_{ij}^k = \frac{1}{A} \Sigma_{k=1}^N m(u_i'^k u_j'^k)$, where A is the area of the computational domain, N is the particle number in the domain, N_k is the contact number of particle k, m is the mass of single particle, r_i^{kl} is the i component of the vector from the center of particle k to particle l, F_j^{kl} is the contact force between these particles and u' is the fluctuation velocity [44]. The contact stress and kinetic stress correspond to two different mechanisms of internal momentum transport, contact transport and streaming transport respectively [46]. For high volume fraction granular material, the kinetic stress is much smaller than the contact stress [46,47]. The solid fraction near the target is so high that the role of kinetic stress can be omitted.

Figures 3(a), 3(b), 4(a), 4(b), 5(a), and 5(b) are the profiles of the time averaged contact stresses in radial and axial directions, respectively, for different sizes of targets with the space between the orifice and the target presented. According to the contact stress profiles, the entire system can be classified into three regions, jet zone, condensed zone, and free zone. The jet zone is the area inside of the tube that the stress is low. The condense zone is the triangular region on the surface of the target with high stress, as shown in Fig. 3(a). The rest region is the free zone, in which the stress is low. There is a critical target size determining the regions classified by the stress profiles. When the target is wider than this critical size, the shape of the condensed zone is an isosceles triangular. The pile angle, ϕ, which is a function of the initial velocity, U_0, does not decrease even when the target becomes wider than the critical value. Figure 3(c) shows the contact stress distribution across a cross-section near the surface of the target where $h=2d$ for both time averaged contact stresses σ_{rr}^c and σ_{hh}^c when $R_{tar}^*=4$. Exponential fits are carried out on the simulated results of σ_{rr}^c and σ_{hh}^c, respectively. The two curves are very close to each other. Both of them can be written as

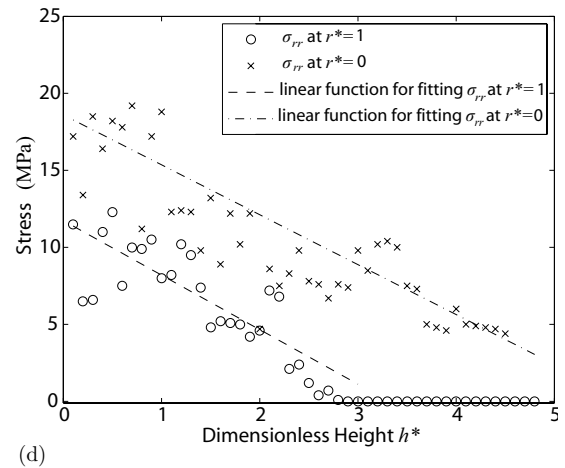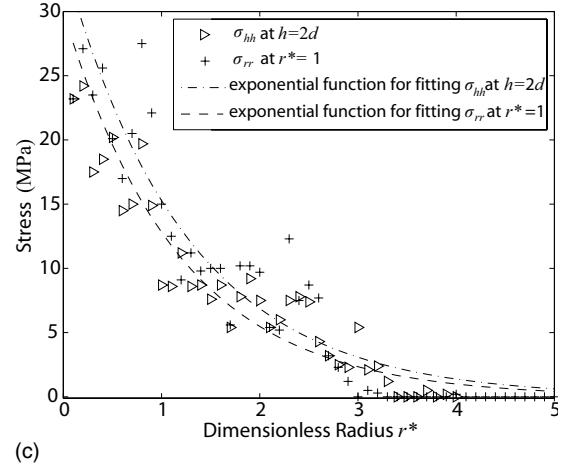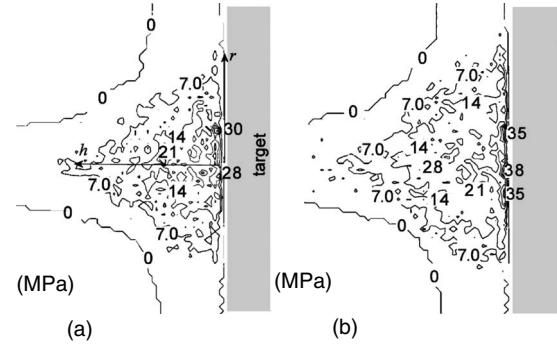$$\sigma_{ij}^c = \sigma_{ij,0}^c \exp\left(-\frac{C}{R_{jet}}r\right), \tag{6}$$

(a)　(b)

(c)

(d)

FIG. 3. Contact stress distribution for $R_{tar}^*=4$: (a) contact stress in radial direction, σ_{rr}^c; (b) contact stress in axial direction, σ_{hh}^c; (c)"+" for σ_{rr}^c, "▷" for σ_{hh}^c at $h=2d$; (d) "□" for σ_{rr}^c at $r^*=0$ and "○" for σ_{rr}^c at $r^*=1$.

where C is a constant and the subscripts $i=j$ indicate the normal stress. Figures 4(c) and 5(c) show the contact stress distribution for $R_{tar}^*=2$ and 1 at the cross-section of $h=2d$. It can be seen that the stress distributions also obey the exponent law given by Eq. (6) when the target becomes smaller. The curves in Figs. 4(c) and 5(c) are the same as the corresponding curves in Fig. 3(c). In addition, the velocity in the axial direction also satisfies conservation of momentum, such that
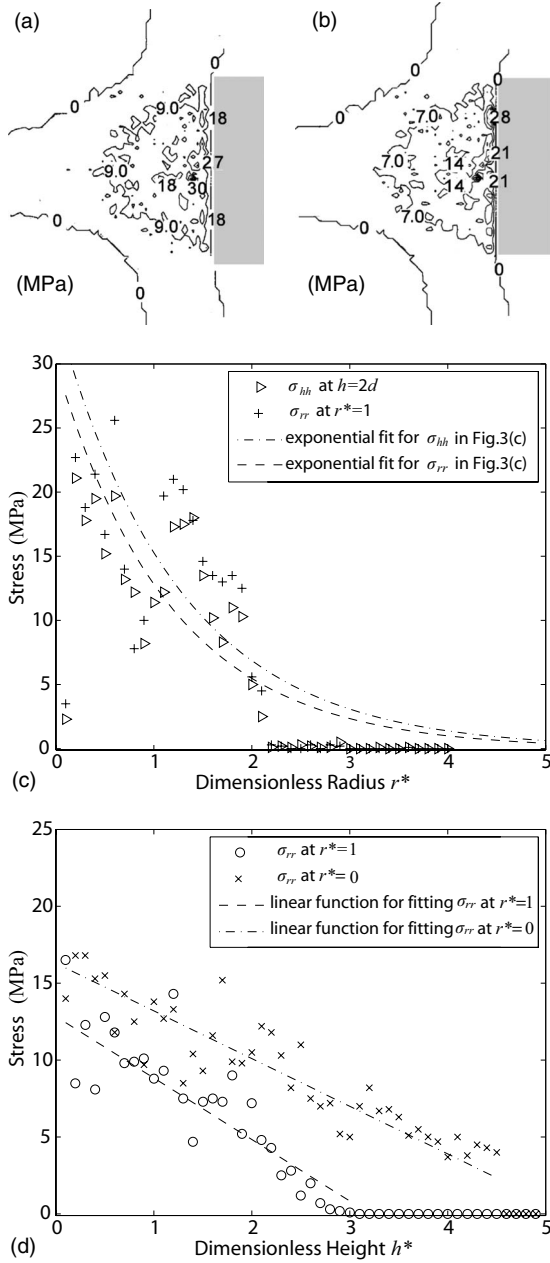
FIG. 4. Contact stress distribution for $R^*_{tar}=2$:(a) contact stress in radial direction, σ^c_{rr}; (b) contact stress in axial direction, σ^c_{hh}; (c)"+" for σ^c_{rr}, "▷" for σ^c_{hh} at $h=2d$; (d) "□" for σ^c_{rr} at $r^*=0$ and "○" for σ^c_{rr} at $r^*=1$.
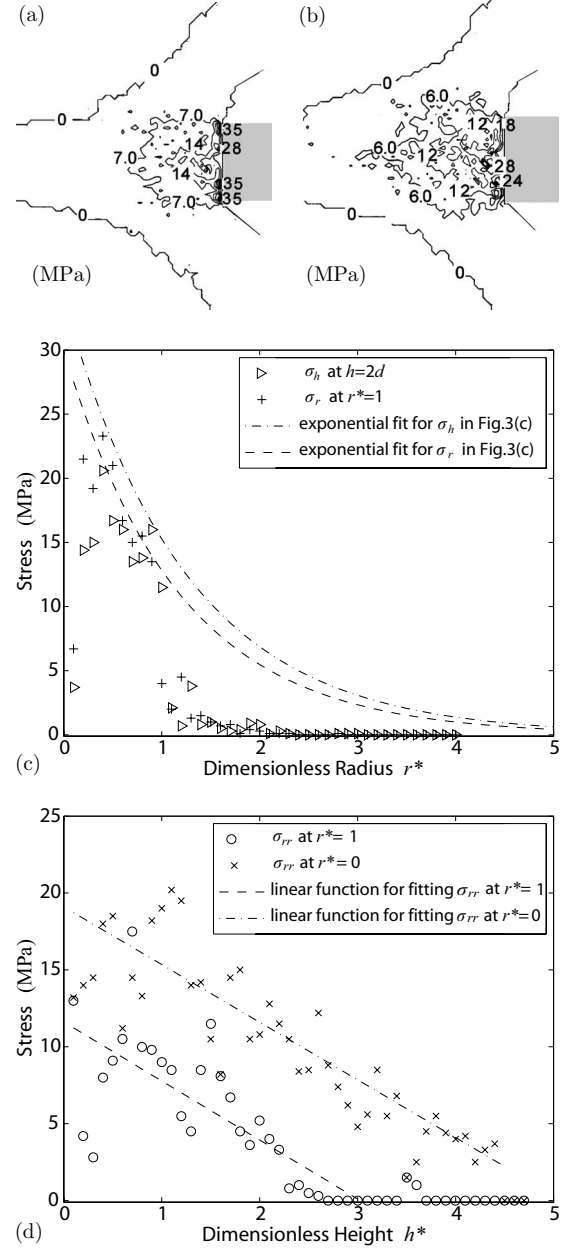

FIG. 5. Contact stress distribution for $R^*_{tar}=1$:(a) contact stress in radial direction, σ^c_{rr}; (b) contact stress in axial direction, σ^c_{hh}; (c)"+" for σ^c_{rr}, "▷" for σ^c_{hh} at $h=2d$; (d) "□" for σ^c_{rr} at $r^*=0$ and "○" for σ^c_{rr} at $r^*=1$.

$$\sum_{i=1}^{N} m_i U'_{h,i} = F_h t + \sum_{i=1}^{N} m_i U_{h,i}\big|_{t=0}, \tag{7}$$

where $U_{h,i}\big|_{t=0}$ means the velocity of the ith particle in h component at time $t=0$, the prime means the state after time, t and N is the particle number in the system. Here, $F_h t$ is sum of the momentum transfer from each particle to the target and the target is considered to have an infinite mass. Hence,

$$QU'_h = F_h + QU_h\big|_{t=0} \tag{8}$$

where Q is the mass rate with unit of kg/s. According to the expression of axial stress σ^c_{hh} in Eq. (6), F_h is also an expo-

nential function of the radius of the target. Thus the relationship between the velocity in the axial component and the size of target is given by,

$$U'_h = U_h\big|_{t=0} \exp\left(-\frac{C}{R_{jet}}R_{tar}\right). \tag{9}$$

Moreover, the radial distribution of σ^c_{rr} is linearly decreasing. Figures 3(d), 4(d), and 5(d) show the contact stress distributions at $r^*=0$ and 2, respectively. The slopes of the lines, which are used to fit the data, are almost the same in these figures. When the surface of the jet flow is simplified with a
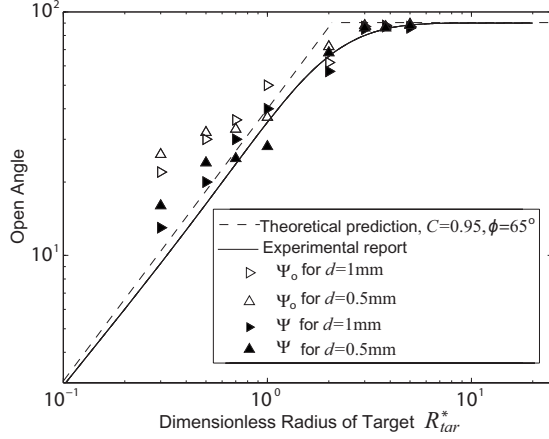
FIG. 6. Relationship between the size of target, R_{tar}^*, and the open angle.

slope $h = h_0 - r \tan \phi$, the averaged contact force at the cross-section of radius $r = r_1$ can be obtained by

$$F_r = \int_0^h \sigma_{rr}^c dh = \sigma_{rr,0}^c (h_0 - r_1 \tan \phi) \exp\left(-\frac{C}{R_{jet}} r_1\right). \tag{10}$$

The radial velocity U_r at $r = 0$ is zero. Due to conservation of momentum, the radial velocity is expressed as

$$U_r' = \frac{F_0 - F_r}{Q}. \tag{11}$$

Substituting the expressions of U_v' and U_h' into the equation for the scattering angle leads to

$$\Psi = \arctan \frac{U_r'}{U_h'}. \tag{12}$$

The results are shown in Fig. 6. It can be seen that $R^* \approx 3$ is the maximum width of the base of the condensed triangular. The experiments [29] show that the two angles are very close to each other for very fine particles, while our simulation indicates that the two angles are different for bigger particles.

V. RESULTS AND DISCUSSION

As discussed above, the overlap is a very important parameter in the DEM simulations. Figure 7 shows the profiles of the time averaged dimensionless overlap in Δ^*, where $\Delta^* = 1000\delta^*$ and $\delta^* = 0.5\delta/d$, for different size of targets in the space between the orifices and the targets. Here, the particles are the same as those shown in Figs. 3–5. According to these profiles, the entire system can be classified into three regions as well as according to the profiles of contact stress. The difference between the profiles of overlap and contact stress is because of the nonlinear characteristic of Eq. (1). The observed maximum instantaneous dimensionless overlap occurs at the very beginning when the jets front arrives at the targets. The value of the maximum instantaneous dimensionless overlap δ_{max}^* is no greater than 0.012 in all of our simu-
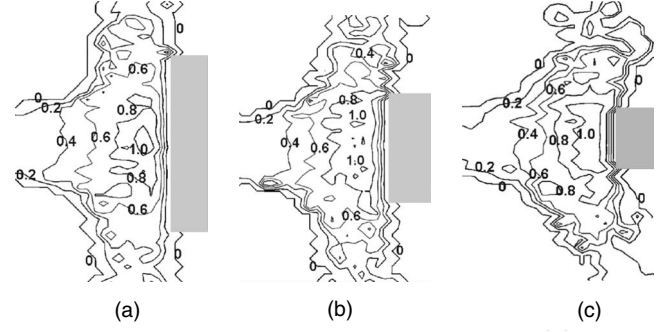

FIG. 7. Time averaged dimensionless overlap in Δ^*, where $\Delta^* = 1000\delta^*$: (a) $R_{tar}^* = 3$; (b) $R_{tar}^* = 2$; and (c) $R_{tar}^* = 1$.

lations. After the condensed zone forming, the maximum instantaneous dimensionless overlap is less than 0.01.

Second, the profile of volume fraction is another interesting aspect in the research of granular flows. The profiles of time averaged volume fraction for different sizes of targets are presented in Fig. 8. It can be seen that the area of high volume fraction (especially, $\phi > 0.9$) increases with the size of the target. The jet and the surface of the target are two regions with very high volume fraction. These two regions link to each other when the target becomes bigger.

Third, our simulations shown in Fig. 2(e) indicates that the characteristic scattering angle θ_{half} is affected by the COR in normal, e. When e is approaching to zero, namely when collision is completely inelastic, the two colliding objects would stick to each other with the same velocity. The target can be considered to be of infinite mass and the result is that the axial velocities of all particles approach to zero. Without any obstacles for the radial velocity, dissipation of radial velocity is much slower than that of axial velocity, thus the granular flow becomes a sheet.

The momentum of any particle at time t can be written as

$$M_t = M_0 + \sum_{i=1}^k \sum_{j=1}^n \Delta M_{i,j}, \tag{13}$$

where M_0 is the initial momentum, $\Delta M_{i,j}$ is the exchange of momentum with jth particle in the ith time step. Here k is the number of time steps from the beginning and n is the total
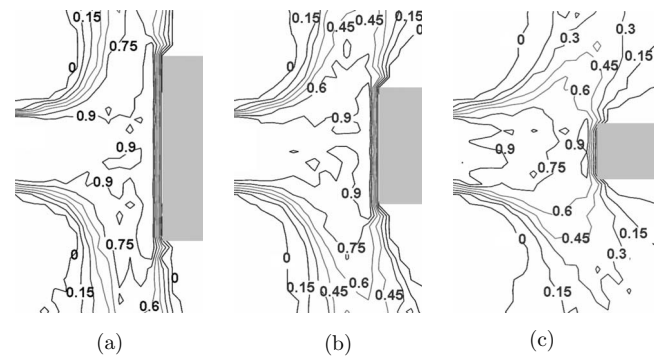

FIG. 8. Time averaged dimensionless volume fraction, $\bar{\Phi}$: (a) $R_{tar}^* = 3$; (b) $R_{tar}^* = 2$; and (c) $R_{tar}^* = 1$.
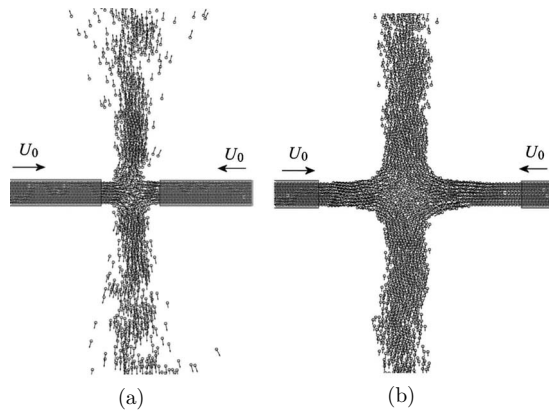
FIG. 9. Head-on collision of two granular jets.

number of particles in contact in the ith time step. Generally, some kinetic energy is lost in the collision and the loss is a function of both COR in normal, e, and relative velocity, U_{12}. The velocity of a particle approaches the same as its neighbors in the dense regime when the number of collisions is sufficiently large. In other words, the local velocity field approaches uniform without energy dissipation among the particles. It should be noticed that the target is modeled as with infinite mass and zero velocity. Hence, the velocities of the particles near the center of the target surface approach zero. When the ratio between d and D_{jet} is decreased, the entire system obtains a higher kinetic energy dissipation rate because the number of collisions increases. On the contrary, if the particles are elastic without friction, there is no energy dissipation in this system and the sheet cannot be formed. Hence the scattering angle is affected by both d/D_{jet} and COR in normal direction, e.

Lastly, when two granular jets collide head-on with the same velocity, our simulations show that the results also depend on the values of d/D_{jet} and e. The particles shown in Figs. 9(a) and 9(b) are the same. As shown in Fig. 9(a), when

the distance between the two nozzles is close, the scattering angle is large, due to the reduced dissipation of kinetic energy. On the other hand, when the distance between two nozzles is further apart, a sheet, at the colliding front, is formed in the middle, as shown in Fig. 9(b). For the cases in which the dimensionless particle size, d/D_{jet}, COR in normal and initial velocity, U_0 are not sufficiently high, a critical distance may be speculated in order to explain the formation of cones or sheets. The value of the critical distance should be dependent on the aforementioned parameters.

VI. CONCLUSIONS

DEM is successfully used to simulate the granular jets hitting on fixed targets with different sizes. The results are in agreement with available experimental data [29,31]. A comparison between the theoretical results based on a kinetic theory type analysis and the present simulation results revealed that the kinetic analyze can be used to predict the neutral angle of scattering, Ψ. In addition, it is found that the sheet-shaped trace is due to the fast kinetic energy dissipation for which the dimensionless particle size, d/D_{tar}, COR in the normal direction, e, and the distance between the orifice and the target play key roles. The DEM simulations are also used to demonstrate the head-on collisions of two opposite granular jets. This case for which no experimental data is available merits further investigations.

ACKNOWLEDGMENTS

[1] J. J. McCarthy, D. V. Khakhar, and J. M. Ottino, Powder Technol. **109**, 72 (2000).

[2] Y. Forterre and O. Pouliquen, Annu. Rev. Fluid Mech. **40**, 1 (2008).

[3] I. Goldhirsch, Annu. Rev. Fluid Mech. **35**, 267 (2003).

[4] J. R. Royer, E. I. Corwin, A. Flior, M.-L. Cordero, M. L. Rivers, P. J. Eng, and H. M. Jaeger, Nat. Phys. **1**, 164 (2005).

[5] M. E. Möbius, X. Cheng, G. S. Karczmar, S. R. Nagel, and H. M. Jaeger, Phys. Rev. Lett. **93**, 198001 (2004).

[6] X. Yan, Q. Shi, M. Hou, K. Lu, and C. K. Chan, Phys. Rev. Lett. **91**, 014302 (2003).

[7] G. Caballero, R. Bergmann, D. van der Meer, A. Prosperetti, and D. Lohse, Phys. Rev. Lett. **99**, 018001 (2007).

[8] GDR MiDi, Eur. Phys. J. E **14**, 341 (2004).

[9] J. R. Royer, D. J. Evans, L. Oyarte, Q. Guo, E. Kapit, M. E. Mobius, R. Waitukaitis, and H. M. Haeger, Nature (London) **459**, 1110 (2009).

[10] H. M. Jaeger, S. R. Nagel, and R. P. Behringer, Rev. Mod.

Phys. **68**, 1259 (1996).

[11] K. To, Phys. Rev. E **71**, 060301(R) (2005).

[12] T. P. C. van Noije, M. H. Ernst, and R. Brito, Physica A **251**, 266 (1998).

[13] P. Zamankhan, Phys. Rev. E **52**, 4877 (1995).

[14] J. T. Jenkins and F. Mancini, Phys. Fluids A **1**, 2050 (1989).

[15] J. T. Willits and B. O. Arnarson, Phys. Fluids **11**, 3116 (1999).

[16] M. Alam, J. T. Willits, B. O. Arnarson, and S. Luding, Phys. Fluids **14**, 4085 (2002).

[17] P. Jalali, M. Li, J. Ritvanen, and P. Sarkomaa, Chaos **13**, 434 (2003).

[18] S. Dartevelle, Geochem., Geophys., Geosyst. **5**, Q08003 (2004).

[19] P. Zamankhan, Phys. Fluids **21**, 043301 (2009).

[20] K. H. Roscoe, Geotechnique **20**, 129 (1970).

[21] S. B. Savage and K. Hutter, J. Fluid Mech. **199**, 177 (1989).

[22] D. V. Khakhar, A. V. Orpe, P. Andresén, and J. M. Ottino, J. Fluid Mech. **441**, 255 (2001).

[23] C. Liu, S. R. Nagel, D. A. Schecter, S. N. Coppersmith, S. Majumdar, O. Narayan, and T. A. Witten, Science **269**, 513 (1995).

[24] D. L. Blair, N. W. Mueggenburg, A. H. Marshall, H. M. Jaeger, and S. R. Nagel, Phys. Rev. E **63**, 041304 (2001).

[25] L. E. Silbert, G. S. Grest, and J. W. Landry, Phys. Rev. E **66**, 061303 (2002).

[26] J. W. Landry, G. S. Grest, L. E. Silbert, and S. J. Plimpton, Phys. Rev. E **67**, 041303 (2003).

[27] J. W. Landry and G. S. Grest, arXiv:cond-mat/0506110 (unpublished).

[28] P. Zamankhan and J. Huang, ASME J. Appl. Mech. **74**, 691 (2007).

[29] X. Cheng, G. Varas, D. Citron, H. M. Jaeger, and S. R. Nagel, Phys. Rev. Lett. **99**, 188001 (2007).

[30] Y. Amarouchene, J. F. Boudet, and H. Kellay, Phys. Rev. Lett. **86**, 4286 (2001).

[31] J. M. N. T. Gray, Y.-C. Tai, and S. Noelle, J. Fluid Mech. **491**, 161 (2003).

[32] R. Ramírez, T. Poschel, N. V. Brilliantov, and T. Schwager, Phys. Rev. E **60**, 4465 (1999).

[33] G. Kuwabara and K. Kono, Jpn. J. Appl. Phys., Part 1 **26**, 1230 (1987).

[34] S. Ji and H. H. Shen, J. Eng. Mech. **132**, 1252 (2006).

[35] P. A. Cundall, *Proceedings of the Symposium of International Society of Rock Mechanics* (Nancy, France, 1971), Vol. 1, p. II.

[36] P. A. Cundall and O. D. L. Strack, Geotechnique **29**, 47 (1979).

[37] C. K. K. Lun and S. B. Savage, J. Appl. Mech. **54**, 47 (1987).

[38] C. K. K. Lun and A. A. Bent, J. Fluid Mech. **258**, 335 (1994).

[39] K. L. Johnson, *Contact Mechanics* (Cambridge University Press, Cambridge, England, 1982).

[40] P. Zamankhan and J. Huang, ASME J. Fluids Eng. **129**, 236 (2007).

[41] H. Hertz, J. Reine Angew. Math. **92**, 156 (1882).

[42] R. D. Mindlin, ASME J. Appl. Mech. **16**, 259 (1949).

[43] H. H. Shen and B. Sankaran, Phys. Rev. E **70**, 051308 (2004).

[44] M. Babic, H. H. Shen, and H. T. Shen, J. Fluid Mech. **219**, 81 (1990).

[45] F. G. Bridges, K. D. Supulver, D. N. C. Lin, R. Knight, and M. Zafra, Icarus **123**, 422 (1996).

[46] C. S. Campbell, Powder Technol. **162**, 208 (2006).

[47] T. Takahashi, *Debris Flow, Mechanics, Prediction and Countermeasures* (Taylor & Francis, London, 2007).